# Solitary waves in a quantum droplet-bearing system

G. C. Katsimiga,[1] S. I. Mistakidis,[2,3] G. N. Koutsokostas,[4] D. J. Frantzeskakis,[4]
R. Carretero-González,[5] and P. G. Kevrekidis[1]

[1]*Department of Mathematics and Statistics, University of Massachusetts, Amherst, Massachusetts 01003-4515, USA*
[2]*ITAMP, Center for Astrophysics | Harvard & Smithsonian, Cambridge, Massachusetts 02138 USA*
[3]*Department of Physics, Harvard University, Cambridge, Massachusetts 02138, USA*
[4]*Department of Physics, National and Kapodistrian University of Athens, Panepistimiopolis, Zografos, Athens 15784, Greece*
[5]*Nonlinear Dynamical Systems Group, Computational Sciences Research Center, and Department of Mathematics and Statistics, San Diego State University, San Diego, California 92182-7720, USA*

(Received 18 February 2023; accepted 26 May 2023; published 15 June 2023)

We unravel the existence and stability properties of dark soliton solutions as they extend from the regime of trapped quantum droplets towards the Thomas-Fermi limit in homonuclear symmetric Bose mixtures. Leveraging a phase-plane analysis, we identify the regimes of existence of different types of quantum droplets and subsequently examine the possibility of black and gray solitons and kink-type structures in this system. Moreover, we employ the Landau dynamics approach to extract an analytical estimate of the oscillation frequency of a single dark soliton in the relevant extended Gross–Pitaevskii model. Within this framework, we also find that the single soliton immersed in a droplet is stable, while multisoliton configurations exhibit parametric windows of oscillatory instabilities. Our results pave the way for studying dynamical features of nonlinear multisoliton excitations in a droplet environment in contemporary experimental settings.

DOI: 10.1103/PhysRevA.107.063308

## I. INTRODUCTION

Multicomponent cold atom macroscopic systems provide the possibility to assess quantum fluctuation phenomena within the weakly interacting regime [1–4]. A recent intriguing manifestation consists of the formation of self-bound quantum droplets owing to the presence of the first-order quantum Lee-Huang-Yang (LHY) correction term [5] acting repulsively in higher than one dimension to prevent the collapse potentially favored by the mean-field interactions. Such states of matter have been originally observed in dipolar gases [6] and afterwards in relevant mixtures [4]. Recently, they were also realized in short-range attractively interacting two-component, both homonuclear [7–9] and heteronuclear [10,11] bosonic mixtures. Other proposals also suggest the existence of these states in Bose-Fermi mixtures [12,13] under the presence of three-body interactions [14–16], optical lattices [17] and spin-orbit coupling [18,19]. Besides atomic platforms, droplet configurations can also be generated, e.g., in photonic systems [20], vapors [21,22], and liquid Helium [23,24], further promoting their broader relevance.

The theoretical modeling of droplets in atomic systems is achieved through an extended Gross–Pitaevskii (eGPE) framework [1,25] which has been utilized to probe a plethora of their properties. In short-range bosonic mixtures that we investigate herein, these include, but are not limited to, their inelastic collisions [26,27], structural deformations from a Gaussian-shape to a flat-top profile [27], the behavior of their collective modes [27–32], the triggering of modulational instability events [33] and their statistical mechanics [34], as well as the effects of thermal instabilities [35–37]. Beyond-LHY correlation effects have also been discussed by considering self-consistently higher-order corrections [38–42] revealing, for instance, slight alterations in the breathing frequency or an enhancement of the expansion velocity.

The focus of the vast majority of the above investigations was on the ground-state properties, collective excitations, and dynamical response of droplets. Yet it is natural, motivated also from corresponding analysis of simpler, mean-field-driven dynamical settings [43], to examine excited states and their dynamical stability in such mixtures. This concerns in particular, the existence of nonlinearity-driven coherent structures, in the form of dark solitons [18,44] and vortices [45–50], as well as vortex rings [51] embedded in these self-bound states, a topic which has been touched upon only very recently. For instance, in the one-dimensional (1D) geometry which is the central focus of the present study, the crossover from dark solitons at weak repulsive couplings to dark quantum droplets at attractive interactions in free space was discussed in Ref. [44]. However, it remains elusive under which conditions dark soliton states persist in the presence of the external trap, a common feature of relevant experiments [7,9,10], and importantly whether additional solutions, e.g., gray solitons [45,52] occur as it was argued recently for dipolar as well as in spin-orbit coupled [53] condensates in the presence of the LHY correction [54]. Additionally, an analytical prediction regarding the dark soliton in-trap oscillation frequency similar to the one known in repulsive condensates [55,56] constitutes a central question.

Another intriguing aspect that we tackle herein concerns the existence, stability, and dynamics of relevant multisoliton configurations, especially so due to the presence of beyond-mean-field nonlinearities in the mixture setting. On a different note, we remark that recently there is renewed interest in

 

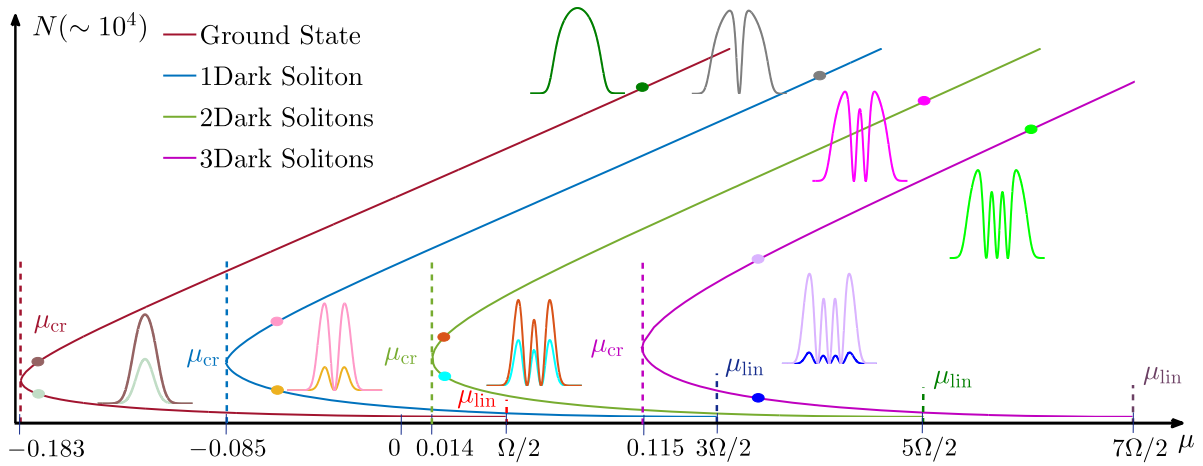


FIG. 1. Schematic representation of the underlying bifurcation diagram of the particle number $N(\mu)$ as a function of the chemical potential $\mu$ for the droplet ground state as well as the single-, two-, and three-droplet dark solitons for $\delta = 1$. Vertical dashed lines indicate the turning point $\mu_{\rm cr}$ and the corresponding linear limit $\mu_{\rm lin} = (n + 1/2)\Omega$ of the adimensionalized model, where $\Omega = 0.1$ denotes the trap frequency. The solution (Hermite-Gauss state) departs from the linear limit and for decreasing chemical potential acquires a droplet background since the LHY dominates until it reaches $\mu_{\rm cr}$. Afterward, the configuration gradually deforms from a Gaussian-type backdrop towards a TF-type backdrop bearing one or more strongly localized dark soliton(s) for increasing $\mu$ where the cubic nonlinearity prevails. Characteristic density profiles of the ensuing localized waveforms at specific chemical potentials (see ellipse markers) are also provided. The latter correspond to $\mu = -0.175$ and 0.115 for the ground states, $\mu = -0.06$ and 0.2 for the single, $\mu = 0.02$ and 0.25 for the two, and $\mu = 0.17$ and 0.3 for the three dark soliton solutions, respectively. Note that for visualization purposes the curves are slightly shifted upwards from $N = 0$. Namely, all the lower curves asymptote to $N = 0$ as $\mu \to \infty$.

the experimental realization of a diverse array of solitonic structures in repulsive condensates [57–61] which is expected to lead to interesting extensions for self-bound droplet environments.

To address the questions posed above we leverage a variety of theoretical and numerical tools. These include (i) a phase-plane analysis of the ensuing dynamical system, (ii) a computational analysis of its excitation spectrum deploying the eGPE framework exploring the regime from the quantum droplet, low-density limit, to the Thomas-Fermi (TF), large-density limit, and (iii) direct numerical simulations in the context of dynamically unstable solutions. Specifically, we consider a homonuclear symmetric bosonic mixture showcasing the existence of various localized solutions in free space. We go beyond the well-studied conventional bright droplets [2,3] and the largely unexplored dark quantum droplets (referred to as bubbles hereafter) [44], examining black [44] and gray solitons [45]. Notice that, while the existence of a fraction of these nonlinear structures has been recently discussed in Refs. [44,45], here we unravel their origin from a completely different perspective. Namely, we rely on solutions of the dynamical system but also expose their persistence in the presence of the trap, as well as investigate their spectrum. The coexistence of multiple of the aforementioned waveforms is elucidated, as are their dynamical properties and the regimes where quantum fluctuations are central to their persistence.

Moreover, utilizing the Landau dynamics approach [62], the LHY-dependent oscillation frequency for a single dark soliton is extracted, recovering the standard mean-field prediction in the appropriate large-density limit [63–65]. Exploring the underlying excitation spectrum reveals that single dark solitons are stable structures for varying chemical potential, trap, and LHY strengths. Strikingly, the interplay between the attractive in 1D LHY term (dominating for small chemical potentials) and the repulsive cubic nonlinearity (prevailing for large chemical potentials) is central for understanding the behavior of solitonic branches. For instance, a dark soliton in this setting bifurcates from the linear limit (either from the band edge in the absence of the trap, or from the first-excited state in its presence) and tends to a "soliton-inside-a-droplet" state for decreasing chemical potentials before turning around so as to acquire a TF-type background for larger chemical potentials. Along these transitions, the dark soliton experiences modifications in its intensity and thus its core size. A summary of the bifurcation structure for the multisoliton configurations is depicted in Fig. 1. It is found that the aforementioned turning point which is a direct imprint of quantum fluctuations depends on the strengths of the LHY term and the trap but also on the soliton number. Turning to the largely unexplored, in this context, multisoliton solutions, we showcase that their turning points are shifted and, importantly, these states experience parametric windows of oscillatory instabilities. These manifest through the amplification of their out-of-phase vibration accompanied by a breathing of the entire configuration.

The content of this work unfolds as follows: Section II introduces the model under investigation and the relevant theory framework based on the eGPE and its hydrodynamic form. Section III unveils the phase-plane analysis of the underlying dynamical system enabling, among others, to identify their in-trap oscillation frequency. In Sec. IV we discuss in detail the excitation spectrum, existence, and stability properties of the single soliton with respect to variations of the chemical potential, the strength of the LHY, and the trap frequency. Section V elaborates on the persistence of multisoliton configurations and unveils their parametric windows of instability.

Finally, in Sec. VI we summarize our results and offer future perspectives and challenges.

## II. ATTRACTIVE BOSE MIXTURE AND ITS HYDRODYNAMIC FORMULATION

We consider a harmonically trapped homonuclear Bose-Bose mixture with equal masses ($m_1 = m_2 \equiv m$) and intraspecies repulsive interactions ($g_{11} = g_{22} \equiv g$). The intercomponent couplings lie in the attractive regime ($g_{12} < 0$), such that droplet configurations are generated depending on the value of the chemical potential. Due to these symmetry considerations it has been argued that the description of the genuine two-component system reduces to an effective single-component system [1,25,27], so that the two components are described by the same wave function, i.e., $\psi_1 = \psi_2 = \psi$. Such a setting has been suggested as accessible to experimental realizations via the utilization of two hyperfine states, $|F, m_F\rangle$, of $^{39}$K, e.g., $|1,-1\rangle$ and $|1,0\rangle$ as it was done in Refs. [7–9]. Nevertheless, we should mention that, although this setting has been considered experimentally in the above works for three-dimensional quantum droplets, we are not presently aware of a genuine 1D experimental realization in the realm of the above model. This remains an important outstanding challenge for the current experimental state of the art.

The corresponding dimensional effective eGPE describing droplet configurations and including the first-order LHY quantum correction [25] has the following form [29]:

$$i\hbar\psi_t = -\frac{\hbar^2}{2m}\psi_{xx} + \frac{\delta g}{2}|\psi|^2\psi - \frac{\sqrt{m}}{\pi\hbar}g^{3/2}|\psi|\psi + V_{\rm tr}(x)\psi, \tag{1}$$

where the subscripts denote partial derivatives, $\delta g = g_{12} + g$ quantifies the deviation from the mean-field balance point $\delta g = 0$ (see the Supplemental material of Ref. [7] for the dependence and controllability of $\delta g$ based on external magnetic fields), and $V_{\rm tr}(x)$ is the (usually parabolic) external trapping potential. The results to be presented in all the figures below are provided in dimensional units in order to be directly comparable with current state-of-the-art experiments. However, for ease of exposition, all the theoretical analysis will be provided using the corresponding adimensional 1D eGPE [25,45]:

$$i\psi_t = -\tfrac{1}{2}\psi_{xx} + |\psi|^2\psi - \delta|\psi|\psi + V_{\rm tr}(x)\psi. \tag{2}$$

Here, energy, time, space, and interaction strength are respectively measured in units of $\mathcal{E}_0 \equiv \hbar\omega_\perp$, $\omega_\perp^{-1}$, $(\hbar/(m\omega_\perp))^{1/2}$, and $(\hbar^3\omega_\perp/m)^{1/2}$. The atomic mass is $m$, and $\omega_\perp$ refers to the confinement frequency in the transversal direction which can be experimentally tuned with the aid of confinement induced resonances [66]. Importantly, the parameter $\delta$ (with $\delta > 0$) describes the "strength" of the LHY contribution [25,45] and is given by

$$\delta = \frac{1}{\pi}\left[\frac{2g^3}{\mathcal{E}_0(g_{12}+g)}\right]^{1/2}. \tag{3}$$

It is evident that $\delta$ depends on the involved interaction strengths (which can be routinely adjusted in the experiment through Fano-Feshbach resonances [7,8,67]) and also on the transverse confinement via $\mathcal{E}_0$. It is a main focus of this work to expose the impact of the LHY "strength" on the solitonic solutions, see for instance Sec. IV. Notice that, for $\delta = 0$, the eGPE reduces to the common Gross–Pitaevskii equation [64,65]. Moreover, we chose a standard parabolic external trapping potential $V_{\rm tr}(x) = (1/2)\Omega^2x^2$, with $\Omega = \hbar\omega_0/\mathcal{E}_0$ and $\omega_0$ is the trap frequency in the longitudinal direction. To restrict the atomic motion in a 1D geometry, where transversal excitations do not play any role, we employ parametric variations in the interval $0 \leqslant \Omega \leqslant 0.1$.

To begin our analysis, we first employ the Madelung transformation [64,68], $\psi = \sqrt{\rho}\,\exp(i\phi)$, where $\rho(x,t)$ and $\phi(x,t)$ denote, respectively, the 1D density and phase of the gas. This way, Eq. (2) is expressed in the following hydrodynamic form:

$$\rho_t + (\rho\phi_x)_x = 0, \tag{4a}$$

$$\phi_t + \tfrac{1}{2}\phi_x^2 + \rho - \delta|\rho^{1/2}| - \tfrac{1}{2}\rho^{-1/2}(\rho^{1/2})_{xx} + V_{\rm tr}(x) = 0. \tag{4b}$$

The above coupled system of equations can be used for the derivation of stationary states of the system in free space [$V_{\rm tr}(x) = 0$], as well as its ground state in the presence of the trap [$V_{\rm tr}(x) \neq 0$].

## III. PHASE-PLANE ANALYSIS

### A. Stationary states in free space

Assuming that the potential $V_{\rm tr}(x)$ can be ignored in order to assess the model properties in free space, we may seek stationary solutions of the form $\rho = \rho(x)$ and $\phi(x,t) = \phi(x)$ for the system of Eqs. (4). In such a case, integrating Eq. (4a) leads to $\phi_x = C_1/\rho$, where $C_1$ is a to-be-determined constant. It is important to note at this stage that the Madelung transformation allows us to identify the gradient of the phase, $\phi_x$, as the velocity of the traveling stationary states under consideration. Therefore, configurations with $C_1 = 0$ correspond to fixed (nontraveling) steady states while the case $C_1 \neq 0$ corresponds to co-traveling configurations.

The equation for $\phi_x$ in conjunction with Eq. (4b) leads to the following expression for the phase:

$$\phi(x,t) = \int \frac{C_1}{\rho(x)}dx - \mu t + \theta_0, \tag{5}$$

where $\mu$ plays the role of the chemical potential and $\theta_0$ is an integration constant. From this expression it becomes evident that the phase of the solution can be determined by the form of $\rho(x)$ (and the constants $C_1$, $\mu$, and $\theta_0$). The density $\rho(x)$, on the other hand, can be found from Eq. (4b), upon substituting the expression (5). Indeed, introducing the auxiliary field $q = \rho^{1/2}$, Eq. (4b) takes the form[1]

$$q_{xx} + 2\mu q + 2\delta|q|q - 2q^3 - \frac{C_1^2}{q^3} = 0, \tag{6}$$

[1]This substitution seems to suggest that $q > 0$. Yet, a careful inspection of the original model leads to the conclusion that $q$ simply needs to be assumed to be real.

which can be viewed as the equation of motion of a unit mass particle in the presence of the effective potential

$$V(q) = \mu q^2 + \frac{2\delta}{3} q^2 |q| - \frac{1}{2} q^4 + \frac{C_1^2}{2q^2}. \tag{7}$$

Notice that integration of Eq. (6) leads to the equation

$$\tfrac{1}{2} q_x^2 + V(q) = E,$$

where $E$ is the total energy of the system. This equation can be readily integrated, resulting in the implicit solution

$$\int \frac{dq}{\sqrt{2[E - V(q)]}} = x - x_0,$$

where $x_0$ is an integration constant. In what follows, we provide a systematic study of the structure of the phase plane $(q, q_x)$ associated with the dynamical system of Eq. (6) focusing, in particular, on localized waveforms $q(x)$ corresponding to homoclinic [i.e., tending asymptotically to the same steady state from the Greek "$\kappa\lambda\iota\nu\omega$" (to tend) and "$o\mu o\iota o$" (same)] or heteroclinic orbits [from "$\kappa\lambda\iota\nu\omega$" and "$\epsilon\tau\epsilon\rho o$" (different), i.e., tending asymptotically to different steady states] in the $(q, q_x)$ plane.

Let us initially, for simplicity, consider the case of nontraveling configurations, $C_1 = 0$. The co-traveling case for $C_1 \neq 0$ is considered for completeness in the Appendix. For $C_1 = 0$, the extrema of the potential, that set the fixed points of the system, are determined by $dV/dq = 0$, i.e., by $q(-q^2 + \delta|q| + \mu) = 0$. To solve this equation, it is necessary to distinguish the cases with $q > 0$ and $q < 0$, and with $\mu < 0$ and $\mu \geqslant 0$. In particular, for $q \geqslant 0$ and $\mu \leqslant 0$, the fixed points are given by

$$q = 0, \quad q_\pm = \tfrac{1}{2}(\delta \pm \sqrt{\delta^2 - 4|\mu|}). \tag{8}$$

This implies that there exist

(a) one fixed point, at $q = 0$, for $\delta^2 < 4|\mu|$,

(b) two fixed points, at $q = 0$ and $q = \delta/2$, for $\delta^2 = 4|\mu|$,

(c) three fixed points, at $q = 0$ and $q = \frac{1}{2}(\delta \pm (\delta^2 - 4|\mu|)^{1/2})$, for $\delta^2 > 4|\mu|$,

while for $q \geqslant 0$ and $\mu \geqslant 0$ there exist two fixed points corresponding to

$$q = 0, \quad q = \tfrac{1}{2}(\delta + \sqrt{\delta^2 + 4\mu}).$$

Finally, in the case of $q < 0$, and due to the fact that the potential is an even function of $q$, the fixed points are mirror symmetric to those above, namely a fixed point $q_{\rm fp}$ for $q > 0$ maps to $-q_{\rm fp}$ for $q < 0$.

The structure of the effective potential and its associated phase plane become particularly interesting when $\mu = \mu_\star = -2\delta^2/9$. For this value, $\delta^2 > 4|\mu_\star|$, and hence there exist five fixed points, namely three saddle points (associated with potential-energy maxima) and two centers (associated with potential-energy minima) at the ordinary differential equation level. The effective potential in this case factorizes as

$$V(q) = -\frac{1}{2} q^2 \left( |q| - \frac{2\delta}{3} \right)^2,$$

and the fixed points share the same energy $E = 0$. The relevant form of the potential (exhibiting two wells at $q = \pm\delta/3$) and the associated phase plane are depicted in Fig. 2(b) for $\delta = 1$. Therefore, for $\mu = \mu_\star$ there exists a quartet of heteroclinic orbits, which correspond to *kink*-type shapes of $q(x)$; see the relevant wave function depicted in red in the bottom panel of Fig. 2(b) and in Fig. 3(b). All these heteroclinic orbits can be found by direct integration, in an explicit analytical form (see, e.g., also Refs. [27,33]), namely,

$$q_{\rm kink}(x) = \pm\frac{\delta}{3}\left[ 1 \pm \tanh\left( \frac{\delta}{3} x \right) \right]. \tag{9}$$

Notice that, inside the eight-shaped pattern that is formed by the quartet of the heteroclinic orbits, periodic solutions are present (that can be expressed in terms of the Jacobi elliptic functions [33]), while outside of this region all trajectories are unbounded. We remark that in the case of $\mu < -\delta^2/4$ for our setting of $\delta = 1$, a straightforward analysis shows that all emergent trajectories $q(x)$ are unbounded for either $x \to +\infty$ or $-\infty$, or both, since there is only a potential-energy maximum at the origin. For $-\delta^2/4 < \mu < \mu_\star$, the situation is akin to the one presented in Fig. 2(a). In this case, that merits separate investigation, there exist homoclinic solutions. However, rather than these being homoclinic to the vanishing background, as the well-studied case of bright droplets, these are homoclinic to the potential maxima at $\pm q_+$, hence representing so-called bubble solutions [69]. Furthermore, even though both bubbles and dark solitons exist on top of a finite background, bubbles do not feature a phase jump (and an accompanying sign change) as dark solitons do. In fact, bubbles are states which commence and return to the same nontrivial equilibrium state (either $q_+$ or $-q_+$) and as such are homoclinic; see the red curve in Fig. 2(a) and also Fig. 3(a). On the other hand, dark solitons commence from one of the nontrivial fixed points (say $q_+$) and end on the other (in this example, $-q_+$, or vice versa starting at $-q_+$ and ending at $q_+$) and, thus, correspond to heteroclinic orbits; see red curves in Figs. 2(c) and 2(d) and also Figs. 3(d) and 3(e). Bubble configurations and their (in)stability will be the subject of a separate study. Indeed, here, as concerns droplets, we will examine solely the bright ones present for $\mu_\star < \mu < 0$ and the dark solitonic excitations potentially present therein.

Turning to $\mu > \mu_\star$, the value of the two maxima of the potential on either side of $q = 0$ increases as $\mu$ increases while the central peak at $q = 0$ remains unchanged. Precisely at $\mu = \mu_\star$ the two side peaks have the same height as the central peak creating the quartet of heteroclinic orbits mentioned above [see Fig. 2(b)]. For larger values of $\mu$, the central peak becomes shallower than the side peaks, resulting in the emergence of a pair of homoclinic orbits to the origin, i.e., the well-recognized bright quantum droplets [27,29,33] [see light blue curves in Fig. 2(c)]. These can be found as exact analytical solutions:

$$q_{\rm droplet}(x) = \mp\frac{3\mu}{\delta} \frac{1}{1 + \sqrt{1 + \frac{9\mu}{2\delta^2}} \cosh(\sqrt{-2\mu} x)}, \tag{10}$$

with the $-$ and $+$ signs corresponding to the homoclinic orbit with $q > 0$ and $q < 0$, respectively, in line with what was reported, e.g., in Refs. [27,29,33] for $\delta = 1$. Notice that,

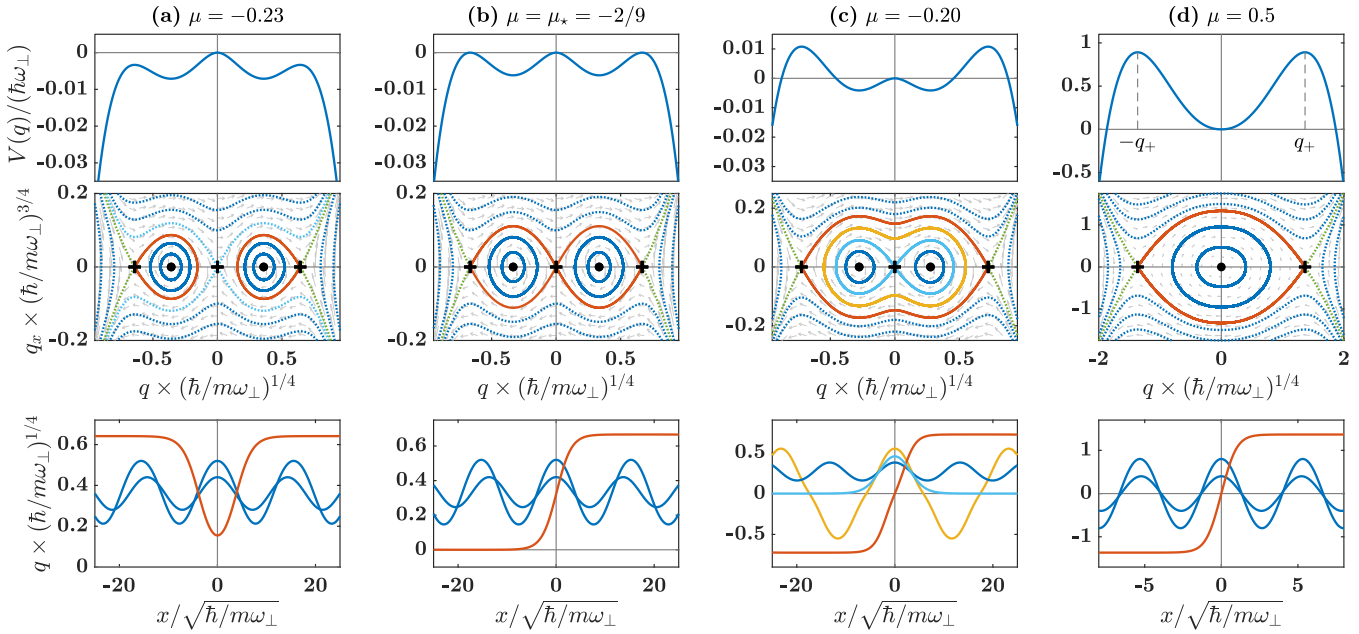


FIG. 2. Potential $V(q)$ (top panels), respective phase planes (middle panels), and bounded orbits (bottom panels) for $C_1 = 0$ and $\delta = 1$ for which $\mu_\star = -2/9$. The different columns of panels correspond to representative cases, for the values of $\mu$ indicated, for all the qualitative different scenarios that produce bounded orbits. Bounded (unbounded) orbits are depicted with solid (dashed) lines in the middle panels. For clarity of exposition, when symmetric ($q \leftrightarrow -q$) solutions exist, only positive bounded orbits are shown in the lower panels. Case (a) corresponds to $-\delta^2/4 < \mu < \mu_\star$ which gives rise to homoclinic orbits supported by a nonzero background. Case (b) corresponds to $\mu = \mu_\star$ where the two homoclinic orbits of case (a) collide and give rise to heteroclinic orbits connecting zero and nonzero backgrounds. Case (c) corresponds to $\mu_\star < \mu < 0$ where the heteroclinic orbits of case (b) merge into heteroclinic orbits connecting nonzero backgrounds. Case (d) corresponds to $\mu > 0$ where the homoclinic orbits of case (c) disappear. Note that, in order to better relate our results to experimental conditions, we opt to display in this figure (as it is the case for all subsequent figures) all of the relevant quantities in full dimensional units as indicated in the labels.

as mentioned above, bright droplets exist within the interval $\mu_\star = -(2/9)\delta^2 < \mu < 0$. A characteristic example of the bright-droplet solution [Eq. (10)] is depicted in Fig. 3(c) [see also the orbit depicted in light blue in Fig. 2(c)]. Obviously, the presence of the LHY term in our extended mean-field model is essential for the existence of such bright droplet waveforms.

Finally, let us focus on the dark soliton solutions. In general, for $\mu_\star < \mu$ (still for $C_1 = 0$), the potential $V(q)$ features two outer extrema $\pm q_+$ associated with a pair of saddle fixed points on either side of $q = 0$ [top panels in Figs. 2(c) and 2(d)]. These outermost saddle fixed points are connected by a pair of heteroclinic orbits producing dark soliton structures, see red curves in the middle and bottom panels of Figs. 2(c) and 2(d). However, as long as $\mu < 0$ there exists also a saddle point at the origin. Due to the presence of this saddle point at $q = 0$, the relevant pair of heteroclinic orbits exhibits a local minimum in $q_x$. As a result, the corresponding dark solitons do not have a tanh-shaped profile as is the case of the usual dark solitons of the defocusing nonlinear Schrödinger equation (NLS) [56], but change their slope in the vicinity of the origin. In fact, due to the bottleneck induced by the effective potential maximum at $q = 0$, the width of the dark soliton may be rendered arbitrarily large in the limit $\mu \to \mu_\star^+$ [44]. A dark soliton profile with an enlarged core is depicted in Fig. 3(d) for $\mu = -0.222$, which should be contrasted with the case when the maximum of the effective potential at $q = 0$ is absent, namely for $\mu \geqslant 0$. In this latter case [see, e.g., Fig. 3(e) for $\mu = 0$], the dark (black) soliton has a profile closer to the familiar tanh-shaped one (with minimum density equal to zero) yet not precisely the same due to the presence of the LHY correction term; see Eq. (11).

Even though the profiles of these dark soliton states are far more complex than the standard NLS dark solitons [56], they can still be obtained analytically for $\delta = 1$ by the following formula:

$$q_{\rm dark}(x) = q_+ + \frac{-\mathcal{B}(\mu) + \sqrt{\mathcal{B}^2(\mu) - 4\mathcal{A}(\mu)\mathcal{C}(\mu)}}{2\mathcal{A}(\mu)}, \quad (11)$$

where $\mathcal{A}(\mu) = B^2 - 4A\tanh^2[\sqrt{A}(x)]$, $\mathcal{B}(\mu) = 4AB\,\mathrm{sech}^2[\sqrt{A}(x)]$, and $\mathcal{C}(\mu) = 4A^2\mathrm{sech}^2[\sqrt{A}(x)]$, with $A = 4\mu + (1 + \sqrt{1 + 4\mu})$ and $B = 2(\frac{1}{3} + \sqrt{1 + 4\mu})$. The expression of Eq. (11) is valid for $x$ such that $q(x) > 0$, while the other "half" of the solution [when $q(x) < 0$] is obtained by antisymmetrizing the wave's profile past the point of its zero crossing. In the above expression, $q_+$ is given by Eq. (8), while it should be noted that for all the solutions discussed in the absence of the trap [cf. also the kinks of Eq. (9) and droplets of Eq. (10)], their invariance with respect to translation allows us to center them at any position $x_0$, even though in the above analytical expressions we have implicitly assumed that they are centered at $x_0 = 0$. Note also that, despite the similarity between the kink structure of Fig. 3(b) and the dark soliton of Fig. 3(e) at the wave function level,

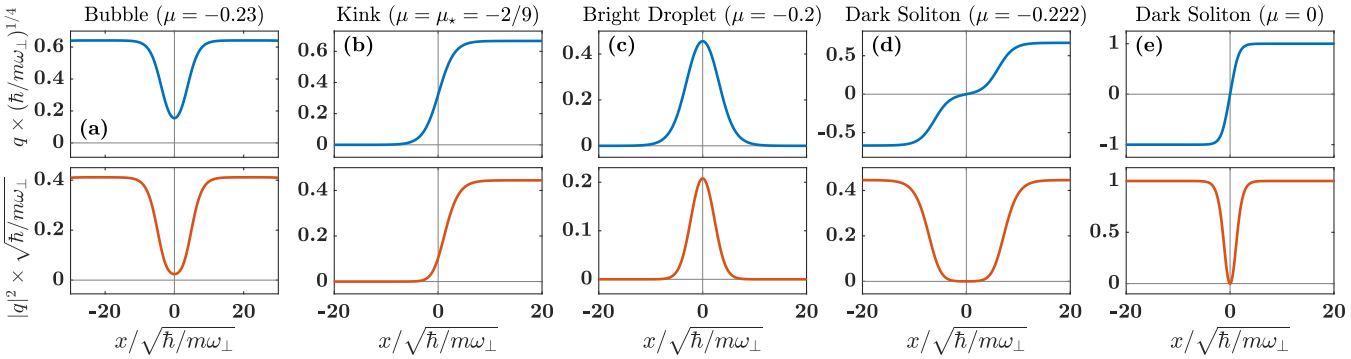


FIG. 3. "Zoo" of nonlinear waves in the crossover from the droplet to the TF regime. Top and bottom sets of panels depict, respectively, the wave function, $q$, and the relevant density profiles, $|q|^2$. (a) Bubble wave function for $\mu = -0.23$ referring to a homoclinic solution anchored at $q_+$. Bubbles are found within the interval $-\delta^2/4 < \mu < \mu_\star$ where $q_+$ exists and $V(0) > V(\pm q_+)$, see also Fig. 2(a). (b) Kink solution corresponding to a heteroclinic connection between 0 and $q_+$ (or $-q_+$), occurring solely for $\mu = \mu_\star = -2\delta^2/9$. Here, the maxima of the effective potential have the same height (energy), i.e., $V(0) = V(\pm q_+)$ [see Fig. 2(b)]. (c) Bright droplet for $\mu = -0.2$. These states form for $\mu_\star < \mu < 0$ when $V(0) < V(\pm q_+)$ and are homoclinic solutions at $q = 0$ [see also Fig. 2(c)]. (d) [(e)] Dark soliton configuration for $\mu = -0.222$ ($\mu = 0$) being a heteroclinic orbit connecting $-q_+$ and $q_+$. These structures arise when $\mu > \mu_\star$ and, as $\mu \to \mu_\star^+$, they become wider due to the bottleneck induced by the potential maximum at $q = 0$ as evinced in panel (d). In all cases, $C_1 = 0$ and $\delta = 1$.

the former solution exists only for $\mu = \mu_\star$ and, additionally, the two states have well distinguished asymptotics.

Summarizing, the systematic analysis of the behavior of the dynamical system associated with the stationary solutions of the eGPE of Eq. (2) for $V_{\rm tr}(x) = 0$ reveals a wealth of localized stationary states. These include bubbles, kinks, bright quantum droplets, dark (black) solitons, and (as discussed in the Appendix) gray solitons. The kink-like structures, bubbles, as well as the bright quantum droplets can only be supported in the system due to the presence of the LHY quadratic nonlinearity term. Notice that periodic nonlinear waves, such as the sn-, cn- and dn-type Jacobi elliptic functions, also exist but are not the focus of this work (see oscillatory, periodic, solutions in the bottom panels of Fig. 2). Moreover, it is particularly relevant to investigate interactions among the above-discussed entities in order to understand their character and whether they bear similarities with interacting solitons. This is discussed in detail in a forthcoming work [70].

### B. The ground state of the trapped system

Let us now consider the ground state of the system in the presence of the external trapping potential $V_{\rm tr}(x) \neq 0$. Within the large-density TF limit, we seek solutions of Eqs. (4) having the form $\rho = \rho_0(x)$, $\phi_t = -\mu$, and $\phi_x = 0$. In this regime, the quantum pressure term $(1/2)\rho^{-1/2}(\rho^{1/2})_{xx}$ can be neglected, and the pertinent ground state is obtained upon solving the reduced Eq. (4b) for $\rho_0^{1/2}$. Namely,

$$|\rho_0^{1/2}(x)| = \frac{\delta}{2} + \left[\left(\frac{\delta}{2}\right)^2 + \mu - V_{\rm tr}(x)\right]^{1/2}, \qquad (12)$$

which is the only relevant solution since $\mu - V_{\rm tr}(x) > 0$. Notice that, in the absence of the LHY term ($\delta = 0$), the well-known form of the TF cloud [64,65] is retrieved. A careful inspection of the solution (12) for the ground state in the large-density limit unveils that it has to vanish for $|x| \geqslant (\delta^2/2 + 2\mu)^{1/2}/\Omega$. An intriguing mathematical question concerns the decay of the trapped state for large $\mu > 0$ towards zero. To address this question, one needs to carefully consider the turning point region where $\mu - V_{\rm tr}(x) \approx 0$. A linear approximation thereof is expected to lead to a variation of the Painlevé-II equation [71] that should be leveraged in order to identify the decay towards vanishing amplitudes. While this is an avenue that we do not pursue herein, we recognize this as a fruitful direction for further mathematical studies associated with the relevant ground state.

Below we focus on the large density limit, investigating the stability spectrum of the ground state since our aim is to embed dark solitons on top of such a background. The stability can be checked upon considering small-amplitude perturbations on the ground-state density $\rho_0(x)$ by substituting in Eqs. (4) the ansatz $\rho(x,t) = \rho_0(x) + \epsilon\rho_1(x,t)$ and $\phi(x,t) = -\mu t + \epsilon\phi_1(x,t)$ where $0 < \epsilon \ll 1$ is a formally small perturbation parameter. In this sense, keeping terms of order $O(\epsilon)$ the following linear equation for $\rho_1(x,t)$ is derived:

$$\rho_{1,tt} - c^2\rho_{1,xx} + \tfrac{1}{4}\rho_{1,xxxx} = 0.$$

The above equation admits plane-wave solutions $\propto \exp[i(kx - \omega t)]$, where the wave number $k$ and frequency $\omega$ obey the Bogoliubov dispersion relation

$$\omega^2 = c^2k^2 + \tfrac{1}{4}k^4, \qquad (13)$$

while $c^2(x) = \rho_0^{1/2}(x)[\rho_0^{1/2}(x) - \delta/2]$ is the square of the local speed of sound [72]. This reveals how the local speed of sound depends on the "strength" of the first-order quantum correction. Note also that the relevant expression is in line with earlier ones for this setting; see, e.g., Eq. (10) of Ref. [51], upon accounting for the density expression of Eq. (12). Therefore, by measuring the speed of sound, it is possible to quantify the presence of quantum fluctuations. Additionally, as dictated by Eq. (13), the frequency is always real for every wave number and thus, as should be expected, the ground state is always stable in the TF limit.

As a final remark regarding the pertinent trapped ground state, it is also of interest to consider its low-density limit in the vicinity of negative chemical potentials, in connection with the relevant continuation illustrated in the bifurcation diagram of Fig. 1. Here, in line with earlier works [45], we see that the trapped ground-state branch does not bifurcate from $\mu = 0$ as in the pure cubic NLS model, but rather starts, as one might expect, from the ground state of the quantum harmonic oscillator at $\mu = \Omega/2$. The effective focusing nature of the model for small or intermediate intensities (due to the dominance for such amplitudes of the quadratically nonlinear term) leads to the formation of a droplet-like state. The latter is strongly reminiscent of the analytically obtained one in Refs. [27,33], yet it is "compressed" in comparison (i.e., narrower) due to the effect of the trapping potential. The resulting branch of solutions accordingly does not have a termination point at $\mu = -2\delta^2/9$. Rather, the corresponding solutions encounter a turning point $\mu_{\rm cr} > \mu_\star$ and subsequently turn and head towards the TF limit discussed above. Indeed, one can identify this turning point as the parametric threshold where the cubic nonlinearity term takes over, eventually leading (for higher values of the chemical potential) to the asymptotic large density regime.

### C. Landau dynamics of dark solitons

In the homogeneous case of $V_{\rm tr}(x) = 0$ and in the absence of the LHY correction, the setting at hand reduces to the completely integrable NLS equation, characterized by the energy

$$H = \int_{-\infty}^{+\infty} [|\psi_x|^2 + (\mu - |\psi|^2)^2] dx. \tag{14}$$

Furthermore, the NLS equation possesses the following exact analytical dark soliton solution [73]

$$\psi(x,t) = \{\sqrt{\mu - v^2}\tanh[\sqrt{\mu - v^2}(x - X_0)] + iv\}e^{-i\mu t}, \tag{15}$$

where $X_0$ is the soliton center and $dX_0/dt = v$ denotes its velocity [43,56]. The energy of the dark soliton can be found upon substituting Eq. (15) into Eq. (14), leading to

$$E_{\rm DS} = \tfrac{4}{3}(c^2 - v^2)^{3/2}, \tag{16}$$

where $c^2 = \mu$ in this limit.

Let us now consider the dynamics of the dark soliton in the TF limit, in the presence of both the LHY term and the external potential. For this purpose, we treat the LHY term as a small perturbation and we assume the potential to be slowly varying on the soliton scale. In such a case, we may employ the so-called Landau dynamics approach [62] (see also Ref. [74]), according to which the soliton energy (14) is treated as an adiabatic invariant in the presence of perturbations. Namely, the background density $\mu$ will be slowly varying according to $\mu \to \mu - V_{\rm tr}(x)$, while $c^2 \to c^2(x) = \rho_0^{1/2}(x)[\rho_0^{1/2}(x) - \delta/2]$ accounting for the LHY contribution.

Then, assuming the adiabatic invariance of the soliton energy in Eq. (16), i.e., $c^2(x) - v^2 = [(3/4)E_{\rm DS}]^{2/3} \approx$ const., using $v = dX_0/dt = \dot{X}_0$ and considering a parabolic trap with strength $\Omega$, namely, $V_{\rm tr}(x) = (1/2)\Omega^2 x^2$, we derive the following nonlinear evolution equation for the dark soliton position:

$$\ddot{X}_0 + \frac{\Omega^2}{2}\left\{1 + \frac{\delta}{4}\left[\frac{\delta^2}{4} + \mu - \frac{1}{2}\Omega^2 X_0^2\right]^{-1/2}\right\} X_0 = 0.$$

Supposing that the soliton motion takes place in the vicinity of the trap center, we extract the oscillation frequency $\Omega_{\rm osc}$ of the dark soliton in the presence of quantum fluctuations as

$$\Omega_{\rm osc} = \frac{\Omega}{\sqrt{2}}\left[1 + \frac{\delta}{4\sqrt{\frac{\delta^2}{4} + \mu}}\right]^{1/2}. \tag{17}$$

Notice that, in the absence of the LHY contribution (i.e., $\delta \to 0$), as well as in the large-density limit (with $\mu \to +\infty$), the oscillation frequency of the dark soliton retrieves the well-known value $\Omega_{\rm osc} = \Omega/\sqrt{2}$ [43,56]. As we will explicate later on, this analytical estimate correctly captures the trend of $\Omega_{\rm osc}$ in terms of $\mu$ as predicted from the numerical solution of the eGPE. However, deviations occur, especially as $\mu$ decreases and as we depart from the TF regime. Indeed, as expected, the relevant frequency in the low-density, near-linear limit tends to $\Omega_{\rm osc} = \Omega$, with the anomalous mode (see the discussion below) interpolating between these two distinctive limits of small and large $\mu$.

## IV. EXCITATION SPECTRUM OF SINGLE DARK SOLITON SOLUTIONS

Having identified through the aforementioned phase-space analysis a plethora of localized solutions that exist in the setup at hand, let us now study stationary single and multiple (see Sec. V) dark soliton solutions in the presence of parabolic confinement [43]. The incorporation of the external trapping potential is of relevance for contemporary experiments [7–9] dealing with homonuclear BEC mixtures. In practice, we obtain the relevant trapped solutions by solving the time-independent version of the eGPE (2) using a fixed point iterative scheme of the Newton type [75].[2] Specifically, stationary states are found upon varying the chemical potential $\mu$, addressing both the small- and large-density (TF) limit for different strengths of the LHY contribution $\delta$ spanning low, intermediate, and comparable to the standard cubic nonlinearity interactions. Characteristic density profiles of the droplet ground state as well as the different single and multiple dark soliton configurations are depicted as insets in Fig. 1.

To address the stability of the above obtained solutions, the following ansatz is introduced in the time-independent eGPE (2):

$$\Psi(x,t) = \{\psi_0(x) + \epsilon[a(x)e^{-i\Omega_{\rm osc}t} + b^*(x)e^{i\Omega_{\rm osc}t}]\}e^{-i\mu t}, \tag{18}$$

where $\psi_0(x)$ is the iteratively found equilibrium solution and $\epsilon$ denotes a small amplitude (formal) perturbation parameter.

[2]For the results presented throughout this work we use a spatial discretization of $dx = 10^{-4}$ with a second-order (cross-checked with the outcome of a fourth-order) finite-difference scheme in space and a fourth-order Runge-Kutta method for the dynamical evolution of the system with temporal discretization $dt = 10^{-5}$.

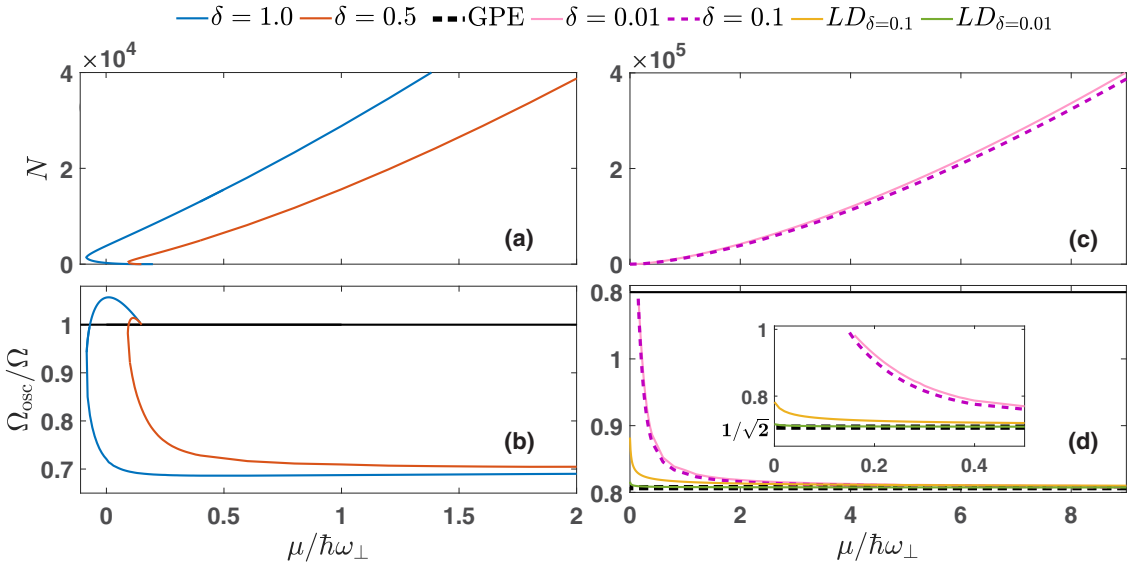


FIG. 4. (a), (c) Bifurcation diagram of the particle number $N$ for the single dark soliton solutions as a function of the chemical potential $\mu$ for different values of the LHY correction as indicated. (b), (d) Corresponding dependence of the internal (anomalous) mode of eigenfrequency $\Omega_{\rm osc}/\Omega$ vs $\mu$. Notice that, in addition to the dipolar mode of frequency $\Omega_{\rm osc}/\Omega = 1$ (see the horizontal black line), the anomalous mode starts from the linear limit $\mu_{\rm lin} = (3/2)\Omega$. As $N$ is increased, for small enough $\delta$ values (see the cases of $\delta = 0.01$ and $\delta = 0.1$), the anomalous mode decreases and then asymptotes to $\Omega_{\rm osc}/\Omega = 1/\sqrt{2}$ for large $\mu$ values [see the horizontal dashed black line in panel (d)]. The inset in panel (d) corresponds to a magnification at small chemical potentials where also the difference from the prediction of Eq. (17) is maximal. In contrast, for large enough values of $\delta$ (see the cases of $\delta = 0.5$ and $\delta = 1$), the anomalous mode frequency first increases and then decreases as $N$ increases while the chemical potential also reaches a turning point for a minimal critical value of $\mu$ at $\mu_{\rm cr}$ ($\mu_{\rm cr} = -0.085$ for $\delta = 1$ and $\mu_{\rm cr} = 0.091$ for $\delta = 0.5$). The trapping strength for all cases is fixed at $\Omega = 0.1$.

Additionally, $\Omega_{\rm osc}$ are the eigenfrequencies and $(a(x), b^*(x))^T$ the eigenfunctions of the eigenvalue problem, which to $O(\epsilon)$ reads

$$\Omega_{\rm osc}\begin{bmatrix} a \\ b \end{bmatrix} = \begin{bmatrix} L_{11} & L_{12} \\ -L_{12}^* & -L_{11} \end{bmatrix}\begin{bmatrix} a \\ b \end{bmatrix}, \tag{19}$$

where $(\cdot)^*$ denotes complex conjugation. Here, the block matrix elements are [29]

$$L_{11} = -\tfrac{1}{2}\partial_x^2 + V_{\rm tr} - \mu + 2|\psi_0|^2 - \tfrac{3}{2}\delta|\psi_0|,$$
$$L_{12} = |\psi_0|^2 - \tfrac{1}{2}\delta|\psi_0|.$$

Notice that the latter expression for $L_{12}$ notably hinges on the fact that the solution $\psi_0$ is real.

Recall, that in the absence of beyond mean-field corrections (i.e., for $\delta = 0$), the dark solitons of the cubic NLS are well known to interpolate between the linear limit of the first-excited state [76,77], with energy $E = \mu = \Omega(n + 1/2)$ for $n = 1$ and the TF limit of large density for large values of the chemical potential $\mu$. Similarly to the ground state of the system (see Sec. III B), the relevant waveform is dynamically stable for all values of $\mu$. However, contrary to what is the case for the ground state, the linearization around such a waveform bears a negative energy (negative Krein signature) [78,79] mode that interpolates between the linear limit of frequency $\Omega_{\rm osc} = \Omega$ and the highly nonlinear TF limit of $\Omega_{\rm osc} = \Omega/\sqrt{2}$ [80]. The Krein signature for the eGPE model under consideration is defined as $K = \Omega_{\rm osc}\int dx(|a|^2 - |b|^2)$. It constitutes a key quantity of the Bogoliubov–de Gennes stability analysis since it identifies the energy contribution of each mode to the unperturbed system. Specifically, depending on the eigenvectors $(a, b)$ such a mode can have a positive frequency $\Omega_{\rm osc}$ but a negative energy $K < 0$ or negative Krein signature. It is these modes that, in what follows, are called anomalous modes (alias negative energy modes).

A natural question here concerns how the relevant bifurcation structure may change in the presence of the quadratic nonlinearity of the LHY term. Indeed, Figs. 4(a) and 4(b) illustrate that the picture is drastically different when the LHY strength is present. Contrary to the defocusing (repulsive) cubic nonlinearity case, which induces a bifurcation towards values of $\mu > E$ (i.e., to the right of the linear eigenvalue of the quantum harmonic oscillator) [43], in the 1D geometry at hand, the focusing (attractive) nature of the LHY [2,42] correction is the dominant one for small intensities. The corresponding bifurcation diagram of the particle number, $N = \int |\psi(x)|^2 dx$, as a function of $\mu$ is depicted in Fig. 4(a) for a pair of values of the LHY correction and a fixed trapping strength $\Omega = 0.1$. As can be seen, for increasing $N$, eventually, the defocusing nature of the large amplitude solutions "takes over" and leads to the emergence of a turning point, for $\delta = 1$, at $\mu = \mu_{\rm cr} = -0.085$. After this turning point, the dependence of $N$ on $\mu$ becomes monotonically increasing, as is representative of a defocusing nonlinearity [43,77]. Interestingly, the relevant critical point when concerning the ground state of the droplet is shifted to more negative values of $\mu$ as compared with the dark droplet soliton solution [see Fig. 1]. Naturally, as the trap strength tends to vanish, accordingly both the starting point of the branch and its $\mu_{\rm cr}$ shift to the left approaching the homogeneous limit values.

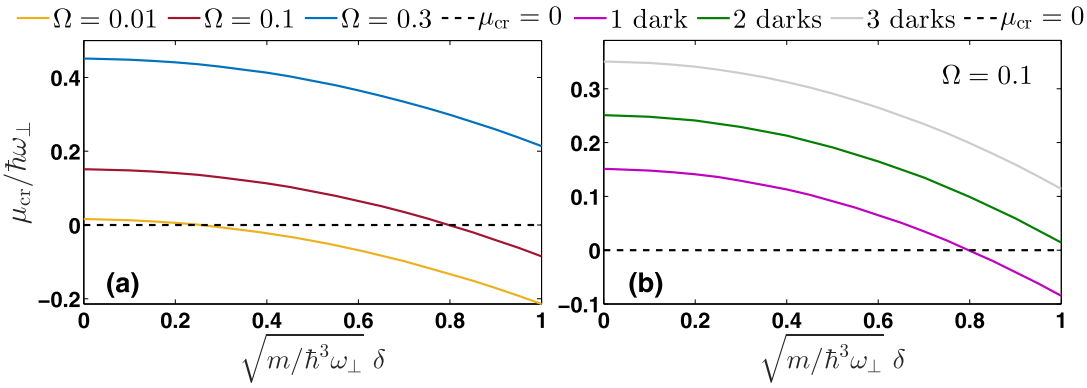


FIG. 5. Critical value of the chemical potential $\mu_{\rm cr}$ versus the LHY strength $\delta$ for (a) single dark soliton solutions and different trap frequencies $\Omega$ (see legend) and (b) distinct dark soliton complexes ranging from one to three (see legend) and for $\Omega = 0.1$. Evidently, for fixed $\delta$ the turning point gets shifted to lower chemical potentials, either by decreasing the trap frequency or the soliton number. In all cases larger $\delta$ reduces $\mu_{\rm cr}$. The dashed horizontal line at $\mu_{\rm cr} = 0$ is added as a guide to the eye.

It is also relevant to follow the dependence of the corresponding "anomalous" (negative energy or negative Krein sign) spectral mode; see Fig. 4(b). The relevant (rescaled) eigenfrequency, at the linear limit bifurcates from the value of $\Omega_{\rm osc}/\Omega = 1$ when $\mu = \mu_{\rm lin} = (3/2)\Omega$. Initially, once again, the effective focusing nature of the nonlinearity leads to larger values of $\Omega_{\rm osc}/\Omega$, but eventually the defocusing character of the large amplitude (high nonlinearity) limit leads $\Omega_{\rm osc}/\Omega$ to turn around and start decreasing as shown in Fig. 4(b). In the large-$\mu$ (TF) limit, the corresponding eigenfrequency asymptotes towards the constant value $\Omega_{\rm osc}/\Omega = 1/\sqrt{2}$. In this latter case, the solution is largely reminiscent of the corresponding cubic problem, while near the linear limit of low density, the solution resembles a first-excited Hermite-Gauss eigenmode; see the relevant profiles in Fig. 1. Indeed, residing on the upper (lower) branch, the soliton core widens for smaller (larger) $\mu$ since the atom number is significantly reduced. The same overall phenomenology occurs also for intermediate strengths of the LHY term as depicted also in Figs. 4(a) and 4(b) for $\delta = 0.5$. Notice however, that for smaller values of the parameter $\delta$, the turning point, appearing at $\mu_{\rm cr} = 0.091$ for $\delta = 0.5$, is shifted towards more positive values.

The significance of the LHY contribution on the stability properties of a single dark soliton is further elucidated by treating this term as a (weak) perturbative one. Namely, when considering significantly lower values of the relevant interaction coefficient such as $\delta = 0.1$ and 0.01; see Figs. 4(c) and 4(d). Evidently, since repulsion prevails in both cases, $N(\mu)$ is a monotonically increasing function as $\mu$ increases from the linear limit of $\mu = 3\Omega/2$; see Fig. 4(c). This monotonicity for small $\delta$ is also present in the relevant dependence of the anomalous mode for each of the distinct values of $\delta$; see Fig. 4(d). In cases of higher $\delta$, as shown in Fig. 4 [see, e.g., Fig. 4(b)], the asymptotics of the relevant anomalous mode still approach the same (scaled) limit of $1/\sqrt{2}$ [as is also predicted by Eq. (17)] for large $\mu$. Yet, they do so through a multivalued $\mu$ dependence, reflecting in this way the corresponding $N(\mu)$ curve. Finally, Fig. 4(d) also depicts the results for the prediction of the dark soliton oscillation frequency using the Landau dynamics approach as per Eq. (17). As the figure suggests, the Landau prediction correctly captures the qualitative tendency of the oscillation frequency for increasingly larger values of $\mu$ albeit with a noticeable discrepancy for small $\mu$ values as depicted in the inset. In that vein, it is relevant to recall that the relevant prediction is expected to be asymptotically valid in the limit of large chemical potential.

Next, we aim to determine the impact of the LHY strength on the location of the critical point of the bifurcation diagram $N(\mu)$ for distinct trap frequencies and soliton numbers. To this end, we initially obtain dark soliton solutions upon varying $\delta$ in the interval $[0, 1]$ covering in this way the small-, intermediate-, and large-density limits and identifying the relevant turning point $\mu = \mu_{\rm cr}$. Focusing on the single soliton case, the behavior of $\mu_{\rm cr}$ in terms of $\delta$ is depicted in Fig. 5(a) not only for $\Omega = 0.1$ that is typically utilized herein, but also upon varying the trapping frequency. It becomes apparent that, irrespective of the trap strength, $\mu_{\rm cr}$ decreases for increasing $\delta$. Additionally, for fixed $\Omega$, $\mu_{\rm cr}$ is shifted to more positive values as $\delta \to 0$ while for looser traps $\mu_{\rm cr} \to -0.2$ for $\delta \to 1$, approaching this way the value of $\mu_\star = -2/9$ found in our previous phase-plane analysis in free space. Furthermore, it is possible to infer from which strength of the LHY contribution onward, $N(\mu)$ features one instead of two (i.e., lower and upper) branches. For instance, when $\Omega = 0.1$ and $\delta \approx 0.2$, $\mu_{\rm cr} \approx \mu_{\rm lin} = 0.15$, and thus for $\delta \lesssim 0.2$ the bifurcation diagram consists only of the upper branch. A similar behavior of $\mu_{\rm cr}(\delta)$ takes place for higher soliton numbers, see in particular Fig. 5(b). As can also be seen, $\mu_{\rm cr}$ is larger for fixed $(\Omega, \delta)$ when increasing the number of solitons; see also the relevant discussion of such solutions in the next section. We remark that, in the absence of a soliton, the respective critical point of the emergent droplet occurs at lower $\mu$, e.g., when $\delta = 1$ then $\mu_{\rm cr} \approx -0.183$; see leftmost curve in Fig. 1.

Since dark solitons and bright quantum droplets can coexist, in what follows we explicitly depict in Figs. 6(a) and 6(b) representative droplet-dark soliton density profiles for different $\mu$ values upon considering variations of the trapping frequency for $\delta = 1$. In all cases, we have verified the spectral stability of these solutions as the homogeneous limit is approached. In line with our previous findings, solutions bearing smaller $\mu$ values, such as $\mu = -0.15$, persist for

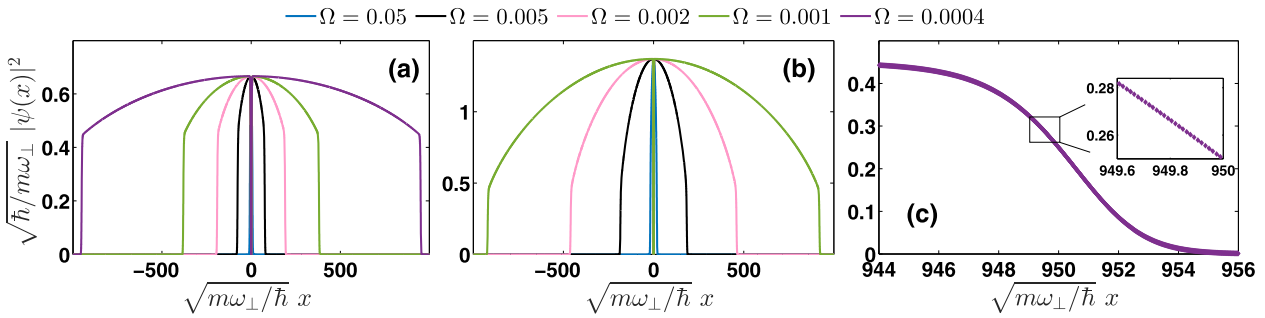


FIG. 6. Selected density profiles of the droplet dark soliton for (a) $\mu = -0.15$ and (b) $\mu = 0.2$ and distinct $\Omega$ values (see legends) in the case of $\delta = 1$. Reducing the trap strength leads to a flat-top droplet dark configuration. Panel (c) and its inset depict different magnifications of the density profile of panel (a) for $\Omega = 0.0004$ illustrating the spatial resolution used.

trap frequencies $\approx 10^{-4}$ but they cease to exist for $\Omega \approx 10^{-2}$. While traversing the relevant branch, the density profiles gradually alter their shape from a configuration proximal to the first-excited Hermite-Gauss eigenstate to a progressively wider dark droplet configuration; see Figs. 6(a) and 6(b). Furthermore, looser traps lead to droplet-dark configurations with a wider flat-top portion, being more pronounced for smaller values of $\mu$. Notice that the droplet background is modified [see Figs. 6(a) and 6(b)] when compared with the homogeneous case [29,44] due to the presence of the trap as has been also observed for dipolar bosons in Ref. [81]. Furthermore, a sharp decay of the density, with respect to the size of the condensate, can be observed at the edge of the cloud. This sharp transition, when compared with the entire domain, forces the numerical characterization of the corresponding solutions to contain a large number of mesh points in order to keep a fine enough discretization to resolve the solution over the entire domain as depicted in the zoomed panel of Fig. 6(c). It is exactly in this turning point region where an analysis tantamount to that of Ref. [71] is relevant to perform, a topic of interest for future mathematical studies.

## V. MULTISOLITON SOLUTIONS AND THEIR DYNAMICS

Let us now consider a homonuclear harmonically confined BEC mixture, in which the LHY contribution is taken on equal footing with the cubic nonlinearity (i.e., $\delta = 1$), and offer a generalization of our findings of the preceding section to multisoliton complexes; see Fig. 1. Note here that, although we restrict ourselves to configurations consisting of two and three dark solitons, our results can be generalized to $\mathcal{N}$-dark soliton states. Starting with a general qualitative remark, we note that higher-order dark solitons (2 solitons, 3 solitons, etc.) are progressively higher excited states of the system; see the relevant discussion of Ref. [82] for the cubic nonlinearity case. As such, each of them bears a progressively higher number of negative Krein-sign eigenvalues. As has been proved in the work of Ref. [83], the number of such negative Krein-sign modes is equal to the number of the solitons in the configuration. While this does not *a priori* render the state dynamically unstable, it renders it far more prone to so-called oscillatory instabilities arising from the collisions of such modes with the rest of the excitation spectrum. The latter, asymptotically, resembles that of the ground-state configuration. In short, an $\mathcal{N}$-dark-soliton state bears $\mathcal{N}$ "excitation modes" (pertaining structurally to in-phase, out-of-phase, and mixed-phase motions of the dark solitons) which may contribute to its potential instability.

The stability analysis outcome of the identified multi-soliton solutions is showcased in Fig. 7. Similarly to the bifurcation diagram of Fig. 4, also here, the dominant attractive role of the LHY term for small $\mu$ values and the repulsive nature of the cubic term for large ones lead to the appearance of a turning point in $N(\mu)$ both for the two- and the three-dark soliton configurations. This turning point appears at $\mu_{\rm cr} = 0.014$ for the two-soliton states while it occurs at $\mu_{\rm cr} = 0.115$ for the three-soliton complexes. However, in contrast with the single dark soliton case, the corresponding spectrum of these higher soliton complexes is more involved as can be seen by inspecting the behavior of the anomalous modes shown in Fig. 7. Here, the lowest-lying anomalous mode (designated by $\mathrm{AM}_1$) for these multisoliton configurations follows a similar trend as the one found in the single dark scenario. This is natural to expect as this mode pertains to the in-phase motion of the dark solitons (see, e.g., Ref. [84]). In this case, the distance between the solitons does not change and hence the oscillation frequency is tantamount to that of the motion of a single soliton in the trap, i.e., effectively of the center of mass. The lowest lying spectral modes depart from the linear limit of $\Omega_{\rm osc}/\Omega = 1$ when $\mu = \mu_{\rm lin} = 5\Omega/2$ and $\mu = \mu_{\rm lin} = 7\Omega/2$ for the two- and three-dark soliton solutions respectively. Additionally, the two and all three anomalous modes turn simultaneously at each of the aforementioned critical points; notice the relevant "loops" present for the second ($\mathrm{AM}_2$) and the second and the third ($\mathrm{AM}_3$) modes for the two- and the three-dark solitons, respectively. In particular, the higher modes for both two- and three-soliton configurations, bearing negative Krein signature ($K < 0$), undergo collisions with the background modes that are characterized by a positive Krein signature ($K > 0$). Such collision events give rise to complex eigenfrequency quartets signaling the presence of an oscillatory instability [79] for the ensuing configuration; see also the discussion in Refs. [43,82,84]. The relevant instability windows for the two-soliton states appear for $\mu \in [0.037, 0.249]$ and $\mu \in [0.482, 0.636]$ whereas they occur for $\mu \in [0.129, 0.349]$ and $\mu \in [0.650, 0.925]$ for the three-soliton states.

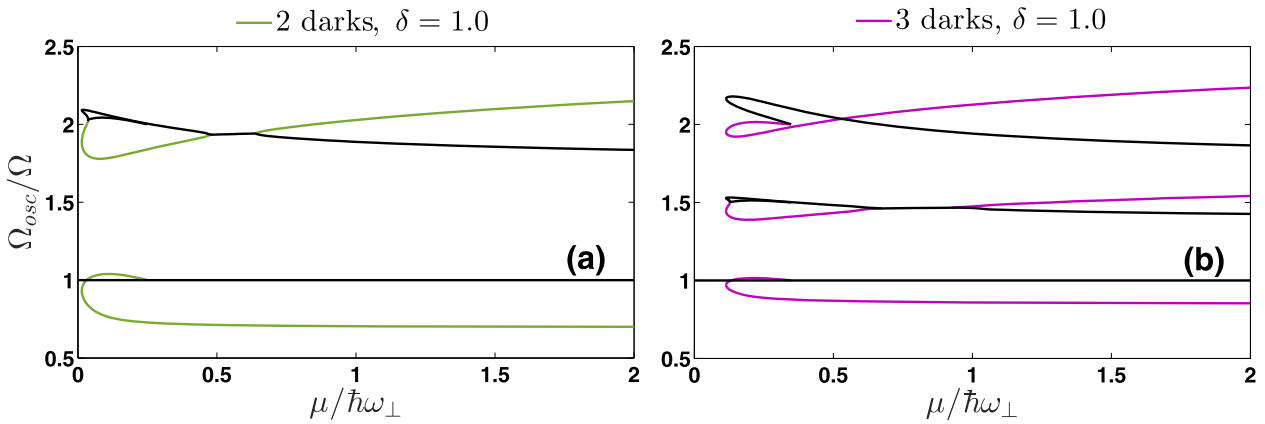


FIG. 7. Dependence of the anomalous mode, $\Omega_{\rm osc}/\Omega$, for (a) two and (b) three dark soliton solutions as a function of $\mu$ for $\delta = 1$. The relevant turning points, being shifted to more positive $\mu$ values for higher soliton complexes, appear at $\mu_{\rm c} = 0.014$ and $\mu_{\rm cr} = 0.115$. In both cases the collision of the second anomalous mode (green and purple lines) with the background ones (black lines) signals the occurrence of an oscillatory instability.

Dynamical evolution of the steady states perturbed by the anomalous modes is showcased in Fig. 8. Specifically, the system is initialized with a perturbed density $|\Psi(x,t)_{\rm AM_i}|^2$ where, as per Eq. (18), the initial condition is given by $\Psi(x,0)_{\rm AM_i} = \psi_0(x) + \epsilon[a_i(x) + b_i^*(x)]$ with the subscript $i$ indicating the anomalous mode number and $\epsilon = 0.3$ is chosen so as to observe the ensuing oscillations already at an early stage within the dynamical simulation. The dynamics of the ensuing anomalous mode perturbations for $i = 1, 2, 3$ of the different multisoliton configurations depicted in Fig. 8 confirms the above stability analysis results, while exposing the internal type of motion that each of the modes induces. Particularly, for both two- and three-soliton states, the lowest lying anomalous eigenfrequency ($\rm AM_1$) leads, once activated, i.e., upon adding to the stationary solution the eigenvector associated with it, to the in-phase vibration of these entities. This is illustrated in Fig. 8(a) [Fig. 8(b)] when $\mu = 1$ ($\mu = 1.5$) and $\delta = 1$ for the two-soliton (three-soliton) configuration. On the other hand, $\rm AM_2$ triggers the out-of-phase oscillation of the two-soliton solution [Fig. 8(c)]. The same type of motion but in a pairwise fashion is activated when exciting the three-soliton state through $\rm AM_3$ [Fig. 8(d)]. The remaining anomalous mode, $\rm AM_2$, in the three-soliton case produces an out-of-phase motion of the outermost dark solitons while the central one is unaffected throughout the evolution (results not shown here). Note that for the stable configurations in Fig. 8, we verified that the evolution remained coherent up to times $t \approx 3 \times 10^3$.

Finally, let us briefly describe the typical dynamics ensuing from the instabilities of multisoliton configurations. Specifically, for parameter values residing in the above-discussed instability windows, we find that, irrespectively of which mode is added to the initially stationary two- and three-soliton configuration, the resonant (unstable) second mode is eventually excited. The activation of this mode is depicted in Figs. 8(e) and 8(f), respectively, for two and three dark soliton solutions and for chemical potentials corresponding to the maximum instability growth rate. Namely, for $\mu = 0.08$ and $\mu = 0.2$ having an imaginary part $\mathrm{Im}(\Omega_{\rm osc}/\Omega) \approx 0.013$ and $\mathrm{Im}(\Omega_{\rm osc}/\Omega) \approx 0.048$, respectively. In both cases, the amplification of the out-of-phase vibration is triggered and progressively leads to an overall breathing of the entire configuration. This overall breathing pattern of the background is more transparent in the three dark soliton state, when compared with the two-soliton one, with the central wave remaining nearly unaffected. The impact of this breathing is also reflected on the occurrence of "beats" present, for instance, at the contraction intervals around $t \approx 700$ or $t = 1650$ in Fig. 8(e). These beats stem from resonances between the anomalous modes of dark solitons and those associated with the background state (on which these solitons are placed). This is a fundamental feature pertaining to such oscillatory instabilities [43].

## VI. CONCLUSIONS AND PERSPECTIVES

We have investigated the existence and stability properties of single- and multisolitonic configurations in the presence of quantum fluctuations as captured by the LHY contribution both in free space and under the influence of a harmonic trap in one spatial dimension. Our analysis covers the regime from the quantum droplet (low density) to the TF (large density) limit. The hydrodynamic formulation of the eGPE describing a homonuclear symmetric bosonic mixture is utilized delivering insights on the existence of localized solutions of the underlying dynamical system.

In free space, the respective phase-plane analysis reveals a variety of localized waveforms such as black and gray solitons, kink-type structures, as well as bright droplets, and the most recently found bubbles. These are identified in the relevant phase portraits as either homoclinic or heteroclinic orbits and analytical solutions for the kinks, the bright droplets, and the dark solitons are discussed. It should be emphasized that kink, bright quantum droplet, and bubble configurations arise exclusively due to the presence of the LHY term.

For harmonically trapped configurations, the so-called Landau dynamics approach which treats the soliton energy as an adiabatic invariant, is employed to obtain a generalized, LHY-dependent, internal oscillation frequency of the dark

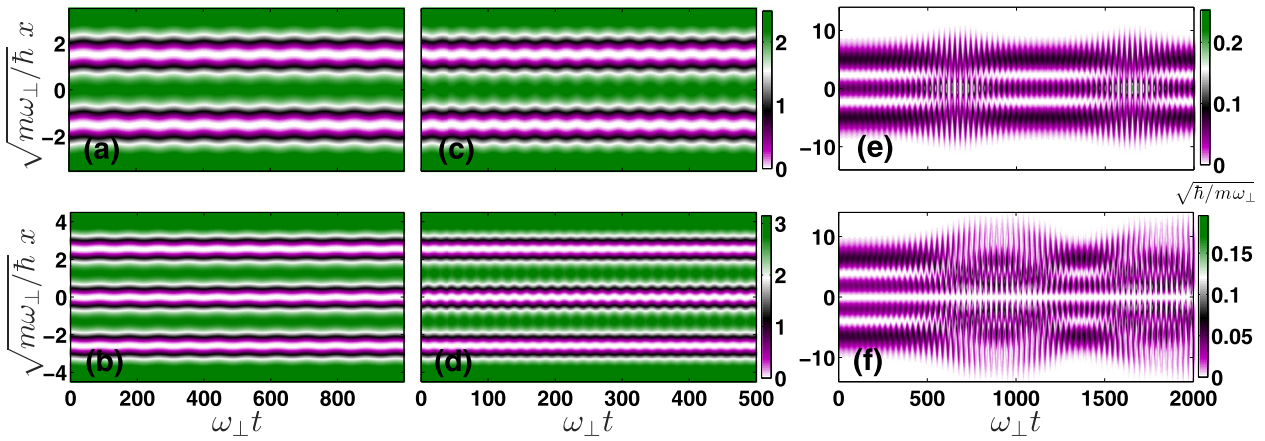


FIG. 8. Density evolution of anomalous modes $|\Psi(x,t)_{\mathrm{AM}_i}|^2$. In each case, the steady state is perturbed with the corresponding anomalous modes initialized with an amplitude of $\epsilon = 0.3$ and then allowed to evolve in time. Panels (a) and (c) [(b) and (d)] correspond to stable modes while panel (e) [(f)] pertains to the unstable mode for the two- [three-] soliton configuration. The anomalous modes in panels (a) and (b) represent in-phase oscillations while panels (c) and (d) correspond to out-of-phase oscillations. The unstable cases depicted in panels (e) and (f) for two and three solitons, respectively, showcase the destabilization of the second anomalous mode ($\mathrm{AM}_2$) through a complex eigenfrequency quartet. It is observed that the dynamical evolution of this instability is manifested as amplified out-of-phase vibrations that eventually saturate and are subsequently subject to recurrence.

soliton. This altered frequency bears the imprint of quantum fluctuations and can be traced back to the already modified local speed of sound, which can be used to diagnose beyond mean-field effects.

The validity of the aforementioned theory is compared with the numerical evaluation of the corresponding eGPE excitation spectrum. In particular, the stability analysis unveils that single dark solitons are stable configurations upon chemical potential and trap variations for different strengths of the LHY interaction parameter. Importantly, the interplay of the LHY (dominating for small chemical potentials) and the cubic nonlinearity (prevailing for large chemical potentials) leads to the existence of a turning point as the number of particles is increased. This turning point is associated with the structural deformation of the configuration from a Hermite-Gauss linear state to a TF-like dark soliton solution, and depends on both the LHY and the trap strength, as well as the soliton number. As such, the presence of the LHY term alters the structure of the dark soliton spectrum as compared with the mean-field outcome providing another imprint of quantum fluctuations. Furthermore, spectral stability is retained for different chemical potentials independently of the trap strength. Multisoliton solutions feature a similar phenomenology as the single dark soliton ones, but with their respective turning points shifted towards more positive chemical potentials for increasing number of solitons in the complexes. Interestingly, multisoliton configurations experience parametric windows of oscillatory instabilities displaying a gradually amplified out-of-phase motion of the individual entities leading to a periodic overall breathing of the entire entity.

There is a plethora of future research directions which can be pursued based on our findings. For instance, a direct extension would be to study in further detail the involvement and influence of dark-droplet states in more practical applications as, e.g., in scattering problems since they are expected to act as material barriers or absorbers. A further understanding of the difference between the analytical prediction of the dark soliton oscillation frequency compared with the eGPE numerical prediction might be fruitful using other perturbation or analytical schemes. It still remains an open question whether the presence of the trap impacts the Bogoliubov modes and thus the LHY term or to what extent higher-order quantum corrections will play a crucial role as argued in Ref. [85]; see also the review of Ref. [42]. Also, it is particularly relevant to extend the present considerations to higher-dimensional settings, e.g., for configurations bearing solitonic stripes where transverse excitations can play a crucial role and induce further instabilities. Certainly, the investigation of soliton and vortex structures and interactions thereof in higher dimensions is of interest. Moreover, the generalization of our results to heteronuclear mixtures where more complex nonlinear structures such as dark-bright and dark-antidark solitons can be formed is another intriguing aspect.

## ACKNOWLEDGMENTS

The work of G.N.K. was supported by the Hellenic Foundation for Research and Innovation (HFRI) under the HFRI Ph.D. Fellowship Grant (Fellowship No. 5860). This material is based upon work supported by the U.S. National Science Foundation under the Awards No. PHY-2110038 (R.C.G), No. PHY-2110030, and No. DMS-2204702 (P.G.K.). S.I.M. gratefully acknowledges financial support from the NSF through a grant for ITAMP at Harvard University. P.G.K. gratefully acknowledges iterations with Mithun Thudiyangal at the early stages of the project.

## APPENDIX: TRAVELING CONFIGURATIONS IN FREE SPACE

To complement the study of nontraveling configurations for $C_1 = 0$ in Sec. III A, here we turn our attention to the case of traveling configurations corresponding to $C_1 \neq 0$ (still in free space, i.e., $V_{\mathrm{tr}} = 0$). In this case, the fixed point at $q = 0$

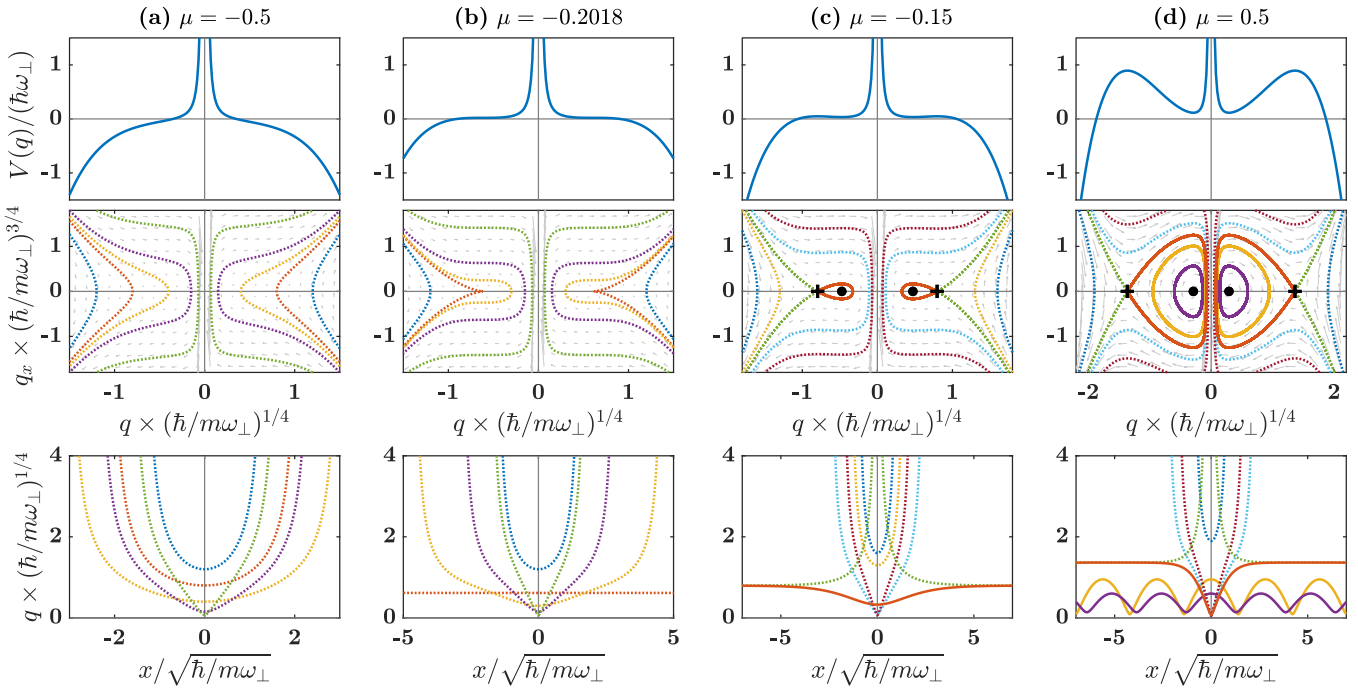


FIG. 9. The potential $V(q)$ (top panels) and respective phase planes (middle panels) and orbits (bottom panels) for $C_1 = 0.1$ and $\delta = 1$. Same layout and notation as in Fig. 2. For (a) $\mu = -0.5$ and (b) $\mu = -0.2018$, all trajectories are unbounded. For values of $\mu$ larger than case (b) ($\mu = -0.2018$) there exist bounded periodic and homoclinic orbits. For example, for (c) $\mu = -0.15$ and (d) $\mu = 0.5$ there exist homoclinic orbits corresponding, respectively, to a shallow and a deep (almost black) gray soliton solution; see the relevant solid red curves in each case.

disappears due to the emergent singularity: in particular, $V(q)$ diverges in the vicinity of $q = 0$; see the top panels in Fig. 9. In this parameter regime, the dynamical system can have zero, two, or four fixed points, depending on the values of $\mu$, $\delta$, and $C_1$.

Since analytical solutions are not straightforward to obtain, we will proceed by providing representative examples corresponding to different values of $\mu$, for fixed $\delta = 1$ and $C_1 = 0.1$. We have checked that other choices of the aforementioned parameters lead to qualitatively similar results. For these parameter values, we find that in the interval $\mu \lesssim -0.2018$, all trajectories are unbounded for $|x| \to \infty$; a pertinent example is given in Fig. 9(a) for $\mu = -0.5$ while the threshold case for $\mu = -0.2018$ is depicted in Fig. 9(b). On the other hand, for larger values of $\mu$, see for instance Figs. 9(c) and 9(d) (corresponding, respectively, to $\mu = -0.15$ and $\mu = 0.5$), center and saddle fixed points on either side of $q = 0$ emerge.

Importantly, in these cases, such an arrangement of fixed points allows for the appearance of homoclinic orbits, with the absolute maximum of $q(x)$ occurring closer to the origin as $\mu$ is increased. The relevant forms of $q(x)$ resemble gray solitons of the usual defocusing NLS equation, which are characterized by a nonzero density minimum. Accordingly, the gray soliton corresponding to the homoclinic orbit for $\mu = -0.15$ depicted in Fig. 9(c) is a shallow one, while the soliton corresponding to $\mu = 0.5$, depicted in Fig. 9(d) is almost black. A detailed study of these gray solitons, including their stability, falls outside of the scope of this work and will be presented elsewhere.

[1] D. S. Petrov, Phys. Rev. Lett. **115**, 155302 (2015).
[2] Z.-H. Luo, W. Pang, B. Liu, Y.-Y. Li, and B. A. Malomed, Front. Phys. **16**, 32201 (2021).
[3] B. A. Malomed, Front. Phys. **16**, 22504 (2021).
[4] F. Böttcher, J.-N. Schmidt, J. Hertkorn, K. S. H. Ng, S. D. Graham, M. Guo, T. Langen, and T. Pfau, Rep. Prog. Phys. **84**, 012403 (2021).
[5] T. D. Lee, K. Huang, and C. N. Yang, Phys. Rev. **106**, 1135 (1957).
[6] L. Chomaz, I. Ferrier-Barbut, F. Ferlaino, B. Laburthe-Tolra, B. L. Lev, and T. Pfau, Rep. Prog. Phys. **86**, 026401 (2023).
[7] P. Cheiney, C. R. Cabrera, J. Sanz, B. Naylor, L. Tanzi, and L. Tarruell, Phys. Rev. Lett. **120**, 135301 (2018).
[8] G. Semeghini, G. Ferioli, L. Masi, C. Mazzinghi, L. Wolswijk, F. Minardi, M. Modugno, G. Modugno, M. Inguscio, and M. Fattori, Phys. Rev. Lett. **120**, 235301 (2018).
[9] C. R. Cabrera, L. Tanzi, J. Sanz, B. Naylor, P. Thomas, P. Cheiney, and L. Tarruell, Science **359**, 301 (2018).
[10] C. D'Errico, A. Burchianti, M. Prevedelli, L. Salasnich, F. Ancilotto, M. Modugno, F. Minardi, and C. Fort, Phys. Rev. Res. **1**, 033155 (2019).
[11] A. Burchianti, C. D'Errico, M. Prevedelli, L. Salasnich, F. Ancilotto, M. Modugno, F. Minardi, and C. Fort, Condens. Matter **5**, 21 (2020).
[12] X. Cui, Phys. Rev. A **98**, 023630 (2018).

[13] D. Rakshit, T. Karpiuk, M. Brewczyk, and M. Gajda, SciPost Phys. **6**, 079 (2019).

[14] Y. Sekino and Y. Nishida, Phys. Rev. A **97**, 011602(R) (2018).

[15] I. Morera, B. Juliá-Díaz, and M. Valiente, Phys. Rev. Res. **4**, L042024 (2022).

[16] S.-L. Xu, Y.-B. Lei, J.-T. Du, Y. Zhao, R. Hua, and J.-H. Zeng, Chaos, Solit. Fractals **164**, 112665 (2022).

[17] X. Zhang, X. Xu, Y. Zheng, Z. Chen, B. Liu, C. Huang, B. A. Malomed, and Y. Li, Phys. Rev. Lett. **123**, 133901 (2019).

[18] S. Gangwar, R. Ravisankar, P. Muruganandam, and P. K. Mishra, Phys. Rev. A **106**, 063315 (2022).

[19] Y. Li, Z. Luo, Y. Liu, Z. Chen, C. Huang, S. Fu, H. Tan, and B. A. Malomed, New J. Phys. **19**, 113043 (2017).

[20] K. E. Wilson, N. Westerberg, M. Valiente, C. W. Duncan, E. M. Wright, P. Öhberg, and D. Faccio, Phys. Rev. Lett. **121**, 133903 (2018).

[21] R. Hołyst, M. Litniewski, D. Jakubczyk, K. Kolwas, M. Kolwas, K. Kowalski, S. Migacz, S. Palesa, and M. Zientara, Rep. Prog. Phys. **76**, 034601 (2013).

[22] J. Feder, K. Russell, J. Lothe, and G. Pound, Adv. Phys. **15**, 111 (1966).

[23] M. Barranco, R. Guardiola, S. Hernández, R. Mayol, J. Navarro, and M. Pi, J. Low Temp. Phys. **142**, 1 (2006).

[24] J. P. Toennies and A. F. Vilesov, Angew. Chem. Int. Ed. **43**, 2622 (2004).

[25] D. S. Petrov and G. E. Astrakharchik, Phys. Rev. Lett. **117**, 100401 (2016).

[26] G. Ferioli, G. Semeghini, L. Masi, G. Giusti, G. Modugno, M. Inguscio, A. Gallemí, A. Recati, and M. Fattori, Phys. Rev. Lett. **122**, 090401 (2019).

[27] G. E. Astrakharchik and B. A. Malomed, Phys. Rev. A **98**, 013631 (2018).

[28] P. Stürmer, M. N. Tengstrand, R. Sachdeva, and S. M. Reimann, Phys. Rev. A **103**, 053302 (2021).

[29] M. Tylutki, G. E. Astrakharchik, B. A. Malomed, and D. S. Petrov, Phys. Rev. A **101**, 051601(R) (2020).

[30] A. Cappellaro, T. Macrì, and L. Salasnich, Phys. Rev. A **97**, 053623 (2018).

[31] H. Hu and X.-J. Liu, Phys. Rev. A **102**, 053303 (2020).

[32] M. N. Tengstrand and S. M. Reimann, Phys. Rev. A **105**, 033319 (2022).

[33] T. Mithun, A. Maluckov, K. Kasamatsu, B. A. Malomed, and A. Khare, Symmetry **12**, 174 (2020).

[34] T. Mithun, S. I. Mistakidis, P. Schmelcher, and P. G. Kevrekidis, Phys. Rev. A **104**, 033316 (2021).

[35] G. De Rosi, G. E. Astrakharchik, and P. Massignan, Phys. Rev. A **103**, 043316 (2021).

[36] J. Wang, H. Hu, and X.-J. Liu, New J. Phys. **22**, 103044 (2020).

[37] A. Boudjemâa, Sci. Rep. **11**, 21765 (2021).

[38] L. Parisi, G. E. Astrakharchik, and S. Giorgini, Phys. Rev. Lett. **122**, 105302 (2019).

[39] L. Parisi and S. Giorgini, Phys. Rev. A **102**, 023318 (2020).

[40] S. I. Mistakidis, T. Mithun, P. G. Kevrekidis, H. R. Sadeghpour, and P. Schmelcher, Phys. Rev. Res. **3**, 043128 (2021).

[41] M. Ota and G. Astrakharchik, SciPost Phys. **9**, 020 (2020).

[42] S. I. Mistakidis, A. G. Volosniev, R. E. Barfknecht, T. Fogarty, T. Busch, A. Foerster, P. Schmelcher, and N. T. Zinner, arXiv:2202.11071.

[43] P. G. Kevrekidis, D. J. Frantzeskakis, and R. Carretero-González, *The Defocusing Nonlinear Schrödinger Equation: From Dark Solitons to Vortices and Vortex Rings* (SIAM, Philadelphia, PA, 2015).

[44] M. Edmonds, arXiv:2209.00790.

[45] Y. V. Kartashov, V. M. Lashkin, M. Modugno, and L. Torner, New J. Phys. **24**, 073012 (2022).

[46] Y. V. Kartashov, B. A. Malomed, L. Tarruell, and L. Torner, Phys. Rev. A **98**, 013612 (2018).

[47] Y. Li, Z. Chen, Z. Luo, C. Huang, H. Tan, W. Pang, and B. A. Malomed, Phys. Rev. A **98**, 063602 (2018).

[48] M. N. Tengstrand, P. Stürmer, E. Ö. Karabulut, and S. M. Reimann, Phys. Rev. Lett. **123**, 160405 (2019).

[49] P. Examilioti and G. M. Kavoulakis, J. Phys. B: At. Mol. Opt. Phys. **53**, 175301 (2020).

[50] M. Caldara and F. Ancilotto, Phys. Rev. A **105**, 063328 (2022).

[51] S. Saqlain, T. Mithun, R. Carretero-González, and P. G. Kevrekidis, Phys. Rev. A **107**, 033310 (2023).

[52] A. Shukla, Neeraj, and P. K. Panigrahi, J. Phys. B: At. Mol. Opt. Phys. **54**, 165301 (2021).

[53] P. Kaur, S. Gautam, and S. K. Adhikari, Phys. Rev. A **105**, 023303 (2022).

[54] J. Kopyciński, M. Łebek, W. Górecki, and K. Pawłowski, Phys. Rev. Lett. **130**, 043401 (2023).

[55] T. Busch and J. R. Anglin, Phys. Rev. Lett. **87**, 010401 (2001).

[56] D. J. Frantzeskakis, J. Phys. A: Math. Theor. **43**, 213001 (2010).

[57] H. Tamura, C.-A. Chen, and C.-L. Hung, arXiv:2211.08575.

[58] S. Mossman, G. C. Katsimiga, S. I. Mistakidis, A. Romero-Ros, T. M. Bersano, P. Schmelcher, P. G. Kevrekidis, and P. Engels, arXiv:2208.10585.

[59] B. Bakkali-Hassani, C. Maury, Y.-Q. Zou, É. Le Cerf, R. Saint-Jalm, P. C. M. Castilho, S. Nascimbene, J. Dalibard, and J. Beugnon, Phys. Rev. Lett. **127**, 023603 (2021).

[60] X. Chai, D. Lao, K. Fujimoto, and C. Raman, Phys. Rev. Res. **3**, L012003 (2021).

[61] A. R. Fritsch, M. Lu, G. H. Reid, A. M. Piñeiro, and I. B. Spielman, Phys. Rev. A **101**, 053629 (2020).

[62] V. V. Konotop and L. Pitaevskii, Phys. Rev. Lett. **93**, 240403 (2004).

[63] P. G. Kevrekidis, D. J. Frantzeskakis, and R. Carretero-González, *Emergent Nonlinear Phenomena in Bose-Einstein Condensates: Theory and Experiment* (Springer, Berlin/Heidelberg, Germany, 2008), Vol. 45.

[64] C. J. Pethick and H. Smith, *Bose–Einstein Condensation in Dilute Gases* (Cambridge University Press, 2008).

[65] L. Pitaevskii and S. Stringari, *Bose-Einstein Condensation and Superfluidity*, International Series of Monographs on Physics (Oxford University Press, Oxford, 2016).

[66] M. Olshanii, Phys. Rev. Lett. **81**, 938 (1998).

[67] C. Chin, R. Grimm, P. Julienne, and E. Tiesinga, Rev. Mod. Phys. **82**, 1225 (2010).

[68] E. Madelung, Eur. Phys. J. A **40**, 322 (1927).

[69] I. Barashenkov, A. Gocheva, V. Makhankov, and I. Puzynin, Phys. D (Amsterdam, Neth.) **34**, 240 (1989).

[70] G. C. Katsimiga, S. I. Mistakidis, B. A. Malomed, D. J. Frantzeskakis, R. Carretero-González, and P. G. Kevrekidis, arXiv:2306.07055.
[71] C. Gallo and D. Pelinovsky, Asymptot. Anal. **73**, 53 (2011).
[72] L. D. Landau and E. M. Lifshitz, *Fluid Mechanics* (Pergamon Press, New York, 1959).
[73] V. E. Zakharov and A. B. Shabat, Zh. Eksp. Teor. Fiz. **64**, 1627 (1973) [Sov. Phys. JETP **37**, 823 (1973)].
[74] P. G. Kevrekidis, W. Wang, R. Carretero-González, and D. J. Frantzeskakis, Phys. Rev. Lett. **118**, 244101 (2017).
[75] C. T. Kelley, *Solving Nonlinear Equations with Newton's Method* (SIAM, 2003).
[76] G. L. Alfimov and D. A. Zezyulin, Nonlinearity **20**, 2075 (2007).
[77] A. Chernyavsky, P. G. Kevrekidis, and D. E. Pelinovsky, *Parity-Time Symmetry and Its Applications* (Springer, 2018), pp. 465–491.
[78] D. V. Skryabin, Phys. Rev. A **63**, 013602 (2000).
[79] G. C. Katsimiga, S. I. Mistakidis, T. M. Bersano, M. K. H. Ome, S. M. Mossman, K. Mukherjee, P. Schmelcher, P. Engels, and P. G. Kevrekidis, Phys. Rev. A **102**, 023301 (2020).
[80] M. P. Coles, D. E. Pelinovsky, and P. G. Kevrekidis, Nonlinearity **23**, 1753 (2010).
[81] S. De Palo, E. Orignac, and R. Citro, Phys. Rev. B **106**, 014503 (2022).
[82] A. Chernyavsky, P. G. Kevrekidis, and D. E. Pelinovsky, Krein Signature in Hamiltonian and PT-Symmetric Systems, in *Parity-time Symmetry and Its Applications*, edited by D. Christodoulides and J. Yang (Springer Singapore, Singapore, 2018), pp. 465–491.
[83] T. Kapitula and P. G. Kevrekidis, Chaos **15**, 037114 (2005).
[84] G. Theocharis, A. Weller, J. P. Ronzheimer, C. Gross, M. K. Oberthaler, P. G. Kevrekidis, and D. J. Frantzeskakis, Phys. Rev. A **81**, 063604 (2010).
[85] I. A. Englezos, S. I. Mistakidis, and P. Schmelcher, Phys. Rev. A **107**, 023320 (2023).